Transition Metal (Co, Ni, Fe) Selenides by Selenization of Gallic Acid based MOFs used as Na-Ion Battery Anodes

Meral Aydin, Thomas Devic, Ali Şems Ahsen, Nicolas Gautier, Rezan Demir-cakan

ChemElectroChem

Research Article
doi.org/10.1002/celc.202400385

Chemistry Europe
European Chemical Societies Publishing

www.chemelectrochem.org

Transition Metal (Co, Ni, Fe) Selenides by Selenization of Gallic Acid based MOFs used as Na-Ion Battery Anodes

Meral Aydin,[a, b] Thomas Devic,[c] Ali Şems Ahsen,[d] Nicolas Gautier,[c] and Rezan Demir-Cakan*[a, b]

Sodium-ion batteries (NIBs) are gaining momentum, thanks to the increasing demand for energy storage devices and the abundant reserves and low sodium cost. Transition metals are well-established materials due to their high conductivity and electrochemical activity. In this work, metal selenides (MSe_x) (M: Ni, Co, Fe) are obtained by facile selenization in a single step of transition gallic acid based metal organic frameworks (MOFs) under Ar flow at 600 °C. As the powders undergo selenization, the resulting MSe_x particles are encapsulated within the amorphous carbon network formed by the decomposition of the gallate ligand. The microstructures are examined by HR-TEM analyses and the characteristic interplanar spacing of each transition metal selenide is measured and found to coincide with the XRD pattern. Meanwhile, the specific surface areas were measured as 121, 152, and 155 m^2/g for $CoSe_2$, NiSe and FeSe, respectively. The resulting NiSe/C, $CoSe_2$/C and FeSe/C nanomaterials are tested as NIB negative electrodes and are shown to have a capacity of 315, 312, and 363 mAh/g, respectively, after 100 cycles at a current density of 100 mA/g while Na-ion diffusion coefficients (D_{Na+}) are calculated in the range of 10^{-10}–10^{-7} cm^2/s by galvanostatic intermittent titration (GITT) technique.

1. Introduction

Lithium-ion batteries (LIB) having high energy density and good cycling capabilities are generally used in many mobile electronic devices, but the scarcity and high cost of lithium pose a challenge.[1,2] Sodium-ion batteries (NIB) are one of the best alternatives to LIBs and they are inexpensive due to their abundant and equitable geographical distribution.[3] However, the large ion diameter of sodium and its slow diffusion ability restrict the electrode material possibilities.

Although a wide variety of negative electrode materials are available, i.e., carbon-based, metal oxide, metal sulfide, and metal selenide, each has its own restrictions.[4] Among them, hard carbon, which works predominantly by adsorption, intercalation, and pore filling mechanisms suffers from low specific capacity and slow kinetics.[5,6] Other electrode materials, i.e. metal oxide, metal sulfide, and metal selenides, have higher specific capacities due to their ability to gain multiple ions, but the common problem of these materials is that they cannot retain the high specific capacities.[7–9] Metal sulphides (MS_x) represent type of anode materials for NIBs, as do metal oxides (MO). Compared to M–O bonds in metal oxides, M–S bonds are of lower energy, which can be kinetically advantageous for conversion reactions in charge-discharge processes.[10] On the selenium side, selenium has been reported to have better cycle stability due to its more metal properties and higher electronic conductivity (~10^{-3} S/m). Therefore, they can be considered as a better alternative compared to sulfide counterparts.[11] However, when metal selenide-based active materials expand and contract during charging/discharging, not only the active material is pulverized and separated from the current collector, but also the SEI is destroyed and repeatedly rebuilt. All these results in the rapid capacity fading of metal selenide anodes.[12] To overcome these challenges, several strategies have been explored such as nanoengineering (structural design),[13] carbon coating,[14] single-atom doping,[15] and heterostructure fabrication.[16] These strategies are expected to improve structural stability and reaction kinetics.[17,18] Regarding carbon doping or coating methods, graphene, carbon nanotubes, carbon nanorods, or hard carbon, as well as metal organic frameworks (MOF) have been employed.

MOF refers to a type of hybrid organic-inorganic polymeric material containing metal ions bonded by poly-complexing organic ligands through complexing groups such as carboxylates, azolates, pyridine, and nitrile groups, defining pores of various shapes and sizes. The broad variety of composition and structure make this family of compounds appealing for numerous applications involving the adsorption and diffusion of guests within the bulk structure.[19] They can also be used as sacrificial precursors to prepare thermal treatment nanostruc-

[a] M. Aydin, R. Demir-Cakan
Gebze Technical University, Department of Chemical Engineering, 41400 Gebze, Kocaeli, Turkey
E-mail: demir-cakan@gtu.edu.tr

[b] M. Aydin, R. Demir-Cakan
Gebze Technical University, Institute of Nanotechnology, 41400 Gebze, Kocaeli, Turkey

[c] T. Devic, N. Gautier
Nantes Université, CNRS, Institut des Matériaux de Nantes Jean Rouxel, IMN, F-44000 Nantes, France

[d] A. Şems Ahsen
Gebze Technical University, Department of Physics, 41400 Gebze, Kocaeli, Turkey

Supporting information for this article is available on the WWW under https://doi.org/10.1002/celc.202400385

tured materials, which were found to be promising for many application areas such as electrochemical storage, catalysts, sensors, etc.[20] Especially, their hybrid nature favors the formation of complex nanostructures, such as carbon-coated inorganic electroactive nanoparticles, with the coating arising from the carbonization of the ligands during annealing in an inert atmosphere. Such structures are of particular interest for electrochemical energy storage, greatly improving the electronic conductivity, enabling rapid Na-ion diffusion, and preventing the destruction of the materials during cycling. In light of all this information, materials derived from MOFs are considered appealing anode materials for NIBs.[21]

The synthesis of new materials using different MOFs is becoming widely used and well-established method nowadays and numerous metal oxide materials have been formed by thermal treatment of MOFs.[22] Upon addition of suitable reactants, MOF-derived metal sulfides,[23] nitrides,[24] and selenides[25] were also prepared. In the last decade, transition metal selenides obtained via MOF selenization have been frequently used in Li/Na-ion batteries.[26,27] Metal selenides can be synthesized by direct selenization of MOFs at high temperatures in an inert medium (Ar)[28] or in Ar/H_2[29] by taking advantage of the reducing property of H_2. Herein, $CoSe_2$/C, NiSe/C, and FeSe/C composites were obtained by one-step pyrolysis of transition metal gallates MOFs mixed with metallic selenium powder at high temperature under Ar atmosphere without additional carbon, and the potential use of the composites as Na-ion battery anode materials was investigated.

Experimental

Materials

Selenium powder was purchased from Alfa Aesar. Sodium perchlorate ($NaClO_4$) (Alfa Aesar), diethylene carbonates (DEC) (Merck), ethylene carbonate (EC) (Sigma-Aldrich), and fluoroethylene carbonate (FEC) (Alfa Aesar) were the electrolyte salts/solvents. Alginic acid sodium (Na-alginate) (Alfa Aesar) was used as a binder. Gallic acid monohydrate and Ni, Co, and Fe salts were purchased from Merck. No other purification of any chemicals has been applied.

Synthesis of MOFs

$M(C_7H_4O_5)\cdot 2H_2O$ (M=Ni, Co) and $Fe(C_7H_3O_5).2H_2O$ were prepared using a room pressure route derived from the one published for the Mg analog.[30] Typically, 3.0 g of gallic acid monohydrate (16 mmol) and 4.0 g of nickel (II) sulfate hexahydrate (15 mmol) were placed in a 250 mL round bottom flask in 40 mL of deionized water. 6.4 mL of a 5 M aqueous KOH solution (32 mmol) was added. The mixture was heated under stirring at 80 °C for a few hours. The resulting solid was recovered by filtration, washed with water and ethanol, and dried in air. For M=Co and Fe, nickel(II) sulfate hexahydrate was replaced by cobalt(II) sulfate heptahydrate and iron(II) chloride tetrahydrate, respectively.

Synthesis of MSe/C Powder

150 mg metal organic frameworks were premixed in an agate mortar for 5 minutes with Se powder at an atomic ratio of 1:3 metal selenium for each M–MOF. The powder mixture was then placed in crucibles and the selenization process was initialized in a tube furnace containing Ar gas. The selenization conditions were set to 600 °C and a ramp rate of 3 °C/min for each sample and held for 3 hours. The samples were cooled down to room temperature naturally and the black samples were collected from the crucible.

Material Characterization

MOF: Routine room temperature Powder X-ray diffraction (PXRD) patterns were collected in a Bragg-Brentano mode with a Bruker D8 Advance diffractometer equipped with a Cu anode and a monochromator ($\lambda = 1.5406$ Å). Thermogravimetric analyses (TGA) were performed under oxygen at 5 °C min^{-1} up to 600 °C on Setaram SENSYSevo equipment. Fourier transformed infrared (FTIR) spectra were recorded at room temperature with a Bruker alpha FTIR spectrometer in the attenuated total reflectance (ATR) mode between 400 and 4000 cm^{-1}.

Metal Selenide/Carbon composites: The phases were analyzed via XRD patterns (Bruker AXS Advance D8 apparatus) with Cu Kα radiation and a scan rate of 1°/min. Scanning electron microscopy (SEM) (Philips XL30) and high-resolution TEM (JEOL JEM 2100F) equipped with a high-angle annular dark-field (HAADF) detector were used to analyze the powders' surface morphologies and the microstructures. STEM-EDX experiments were carried out using a Themis Z G3 Cs-probe corrected microscope from Thermo Fisher Scientific, operating at 300 kV. High-angle annular dark field (HAADF) images were acquired with an 18.6 mrad convergence angle and 65–200 mrad collection angles and EDX maps with 4 windowless silicon drift detectors (Super-X system). The solid suspended in ethanol was deposited onto a lacey carbon film supported by a copper grid. Thermogravimetric analysis (TGA) (Mettler Toledo TGA/SDTA 851) measurement was performed between 30 and 900 °C at a heating rate of 10 °C/min under an air atmosphere. X-ray Photoelectron Spectroscopy (XPS) measurements were carried out in the UHV chamber equipped with a SPECS Phoibos 150 charged particle analyzer and SPECS XR 50 X-ray source (Al Kα). The chamber has a base pressure of about 2.0×10^{-10} mbar.

Electrochemical tests: For the slurry, metal selenide/carbon powder and super P were ground by hand in an agate mortar and pestle for 5 minutes, followed by the addition of sodium alginate binder at a mass ratio of 8:1:1. The slurry was stirred overnight with a magnetic stirrer and coated on Cu foil and dried overnight in a vacuum oven at 80 °C. The active material mass loading was around 0.8–1.2 mg/cm^2. The electrolyte composition is 1 M $NaClO_4$ in ethylene carbonate (EC) and diethylene carbonate (DEC) with 5 wt. % fluoroethylene carbonate (FEC) additives. 0.1 ml of electrolyte was used for the Swagelok (BioLogic) and 0.12 ml for the coin cell (Neware). Whatman GF/D glass was used as a separator. The voltage window, where sodium metal was used as both reference and counter electrodes, was selected from 0.01 to 3 V (vs. Na/Na^+) for the galvanostatic and cyclic voltammetry test. The capacity values were reported per gram electrode (MSe_x/C). The CV scan rate was 0.1 mV/s. Electrochemical impedance tests were done between 10 mHz and 100 kHz with a voltage amplitude of 5 mV in a two-electrode via Biologic VMP-3 galvanostat/potentiostat. Galvanostatic intermittent titration technique (GITT) tests were performed via discharge/charge process with 20 min galvanostatic discharge/charge and 2 h open circuit rest at a current density of 50 mA/g.

2. Result and Discussion

Among the MOFs available, we selected one structure type, M-gallate, which is a microporous MOF that can be easily prepared with a great variety of metallic (M) cations, including Ni(II), Co(II) and Fe(III).[31–33] This solid is synthesized in water at room pressure from a metallic salt and gallic acid, which is an abundant natural phenolic compound found in tea, fruit, coffee, and other foods.[34] As shown in Figure S1, powder XRD, infrared spectroscopy and thermogravimetric analyses are consistent with the targeted structure and compositions. These solids were further treated with selenium at 600 °C. XRD analysis given in Figure 1 was performed for Co, Ni, and Fe selenide materials synthesized under the same conditions to determine crystalline phases. The main peaks are assigned to the corresponding $CoSe_2$ (PDF#009-0234), NiSe (PDF#002-0892), and FeSe (PDF#075-0608) phases,[35–37] while no peak characteristic of the MOF is found, confirming its full conversion into metal selenide. To compensate for the loss of selenium during annealing (as selenium has a relatively low melting point of 221 °C and some of it will vaporize), more than the stoichiometric ratio of selenium powder was used to react with the metal present in the MOF. Therefore, at the end of the selenization process, trace amounts of unreacted selenium peaks in each metal selenide can be seen in the XRD pattern. Crystallite size calculations were determined as 22 nm, 35 nm, and 28 nm based on the main peaks at 34°, 33°, and 32° using the Debye-Scherrer equation (Eq. 1), where X-ray wavelength λ value is 0.1541 nm, Scherrer constant k value is 0.9 for Cu Kα, and d is the full width at half maximum intensity and θ is the peak position.

$$D = \frac{\lambda k}{d\cos\Theta} \quad (1)$$

In addition, the carbon contents of the materials were determined after selenization by TGA analysis under the air atmosphere given in Figure S2a, d, and g. Up to 400 °C, a small mass increase was observed due to partial oxidation of all samples.[38,39] At higher temperatures, mass loss occurs due to decomposition of the metal selenide and sublimation of SeO_2, which has a relatively low melting temperature (350 °C).[40,41] The TGA analysis was halted at a temperature of 500 °C. Upon analyzing the XRD patterns, a mixture of metal oxide and metal selenide was detected (Figure S2b, e, and h). All compounds were ultimately transformed into the oxide phase in the residues at 900 °C (Figure S2c, f, and i). From the TGA curve carbon content of the samples are calculated as ~9%, 27% and 28% for $CoSe_2$/C, NiSe/C, and FeSe/C, respectively.[36,37] The specific surface areas of $CoSe_2$/C, NiSe/C and FeSe/C materials were calculated as 121 m^2/g, 152 m^2/g, and 155 m^2/g, respectively, according to Braunner-Emmet-Teller (BET) analyses given in Figure S3a. According to the isotherm classifications made by IUPAC, N_2 adsorption/desorption isotherms correspond to Type IV hysteresis H4.[12,42] Furthermore, Barrett-Joyner-Halenda (BJH) analysis revealed the presence of small mesopores of similar size (~3–4 nm) in all solids (Figure S3b).[41]

SEM and (HR)TEM were applied to evaluate the structure morphology of the resulting samples. From the SEM images imaging (Figure 2a–c) all the samples are composed of similar ultrafine sphere-like particles. As shown in Figure 2d–f, TEM analyses revealed that these secondary particles consist of metal selenide nanoparticles of ~10–30 nm diameter embedded in a carbonaceous matrix arising from the carbonization of the organic ligands. This composite structure was further confirmed by the STEM-EDS analysis on the Fe derivative (Figure S4).[43] The interplanar spacing for each sample (given in Figure 2d–f) measured by HR-TEM as 0.26 nm for the $CoSe_2$ (210) plane, 0.26 nm for the NiSe (101) plane, 0.28 nm for the FeSe (101) plane. The HR-TEM measurement for Co and Ni samples overlap with SAED measurement, and it also coincides with the literature for Ni and Co-based materials.[44,45] While the d-spacing calculated from SAED deviates from the HR-TEM calculation.[46] Furthermore, at low magnification, the energy dispersive X-ray (EDX) mapping (in Figure 2j–l) shows the distribution of the elements metal (pink), selenium (green), and carbon (blue).

X-ray Photoelectron Spectroscopy (XPS) of the metal selenides obtained from the selenization of MOFs was performed to investigate both elemental analysis and chemical binding states of the elements given in Figure 3. Figure 3a shows the peaks of photoelectrons from the 2p energy level of Co. Here, the energies of the photoelectrons appears as $2p_{1/2}$ and $2p_{3/2}$ energy levels due to spin-orbit interaction.[47] As a result of the fit studies on Co peaks, the peaks at 778.55 eV and

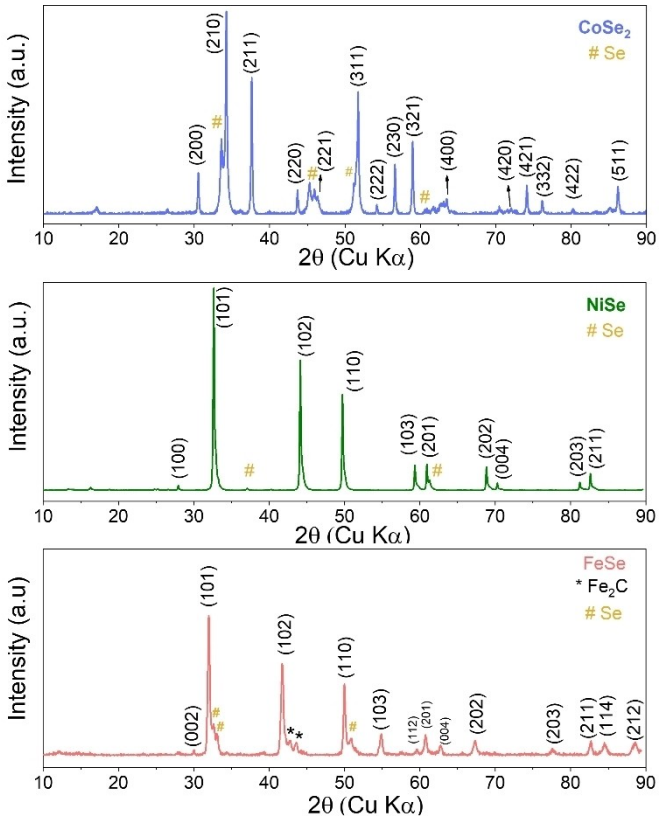

Figure 1. XRD pattern transition metal (Co, Ni, Fe) selenides/carbon composites, **a**) $CoSe_2$/C, **b**) NiSe/C and **c**) FeSe/C.

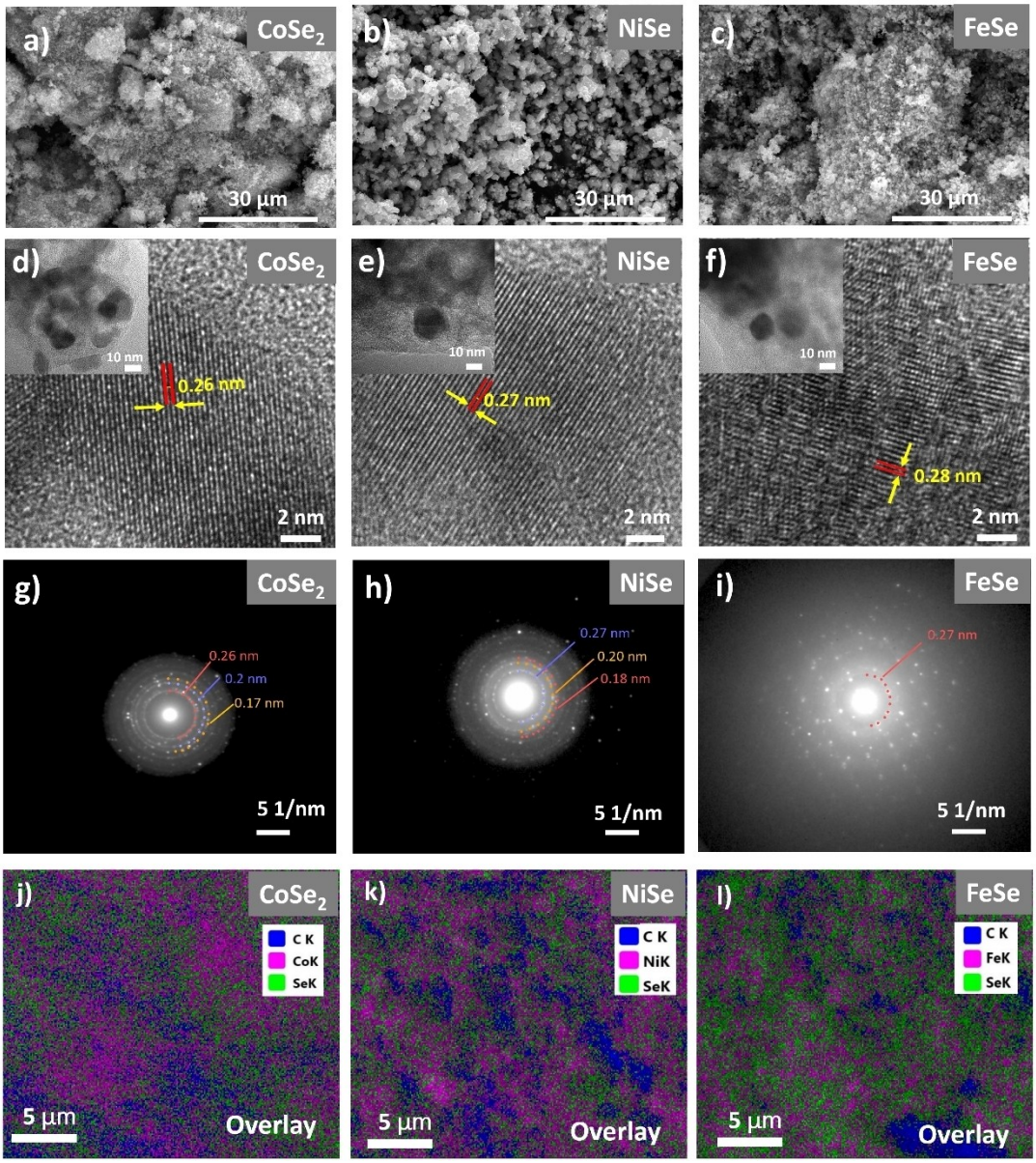

Figure 2. Morphologies of Co, Ni, and Fe Selenides. **a**–**c**) SEM images, **d**–**f**) HR-TEM images, **g**–**i**) SAED pattern, and j-l) mapping of electrode surfaces.

793.49 eV corresponds to Co–O bond of Co $2p_{3/2}$ and Co $2p_{1/2}$, respectively,[47] while the photoelectrons with binding energies of 781.07 eV and 796.56 eV is attributed to Se–Co–Se bond of Co $2p_{3/2}$ and Co $2p_{1/2}$.[48] These are followed by satellite peaks with binding energies of 786.76 eV and 802.25 eV.[49] In the high-resolution Se 3d spectrum obtained from the $CoSe_2$/C sample (Figure 3b), photoelectrons with binding energies of 54.57 eV (Se $3d_{3/2}$) and 55.43 eV (Se $3d_{5/2}$) are attributed to Co–Se, whilst 55.97 eV (Se $3d_{3/2}$) and 56.83 eV(Se $3d_{5/2}$) belong to metallic selenium.[50–52] In addition, the peaks at 59.04 eV and 60.20 eV are attributed to Se–O peak and Co 3p due to surface oxidation by air contact, respectively.[12,53] The peaks 284.39 eV, 284.78 eV and 286.43 eV obtained in the C 1s high-resolution spectrum of $CoSe_2$/C material are associated with sp^2 C=C, sp^3 C–C and C–O bonds, respectively (Figure 3c).[54] The sub-peaks at 853.04 eV and 870.31 eV binding energies were formed after fitting the Ni $2p_{3/2}$ and Ni $2p_{1/2}$ peaks occurred due to the Ni–Se interaction in the NiSe/C sample (Figure 3d). The spectra of metallic nickel, which are strikingly similar those of Ni $2p_{3/2}$ (853.04 eV) and Ni $2p_{1/2}$ (870.31 eV), are shifted to binding energies as high as 0.2–0.3 eV.[55,56] Photoelectrons with energies of 856.16 eV and 873.46 eV are explained by the Ni–O structure formed as a result of surface oxidation similar to the $CoSe_2$/C sample.[57] The high-resolution spectrum of Se 3d was analyzed by fit study. Two peaks at 54.43 eV and 55.29 eV, corresponding to Se $3d_{5/2}$ and Se $3d_{3/2}$, respectively, are attributed to the selenium-nickel bond structure.[58,59] The peaks with binding energies of 56.21 eV and 57.07 eV corresponded to unreacted metallic selenium and the peak at 59.13 eV corresponded to SeO_x (Figure 3e).[60] The 284.53 eV and 284.95 eV peaks in the

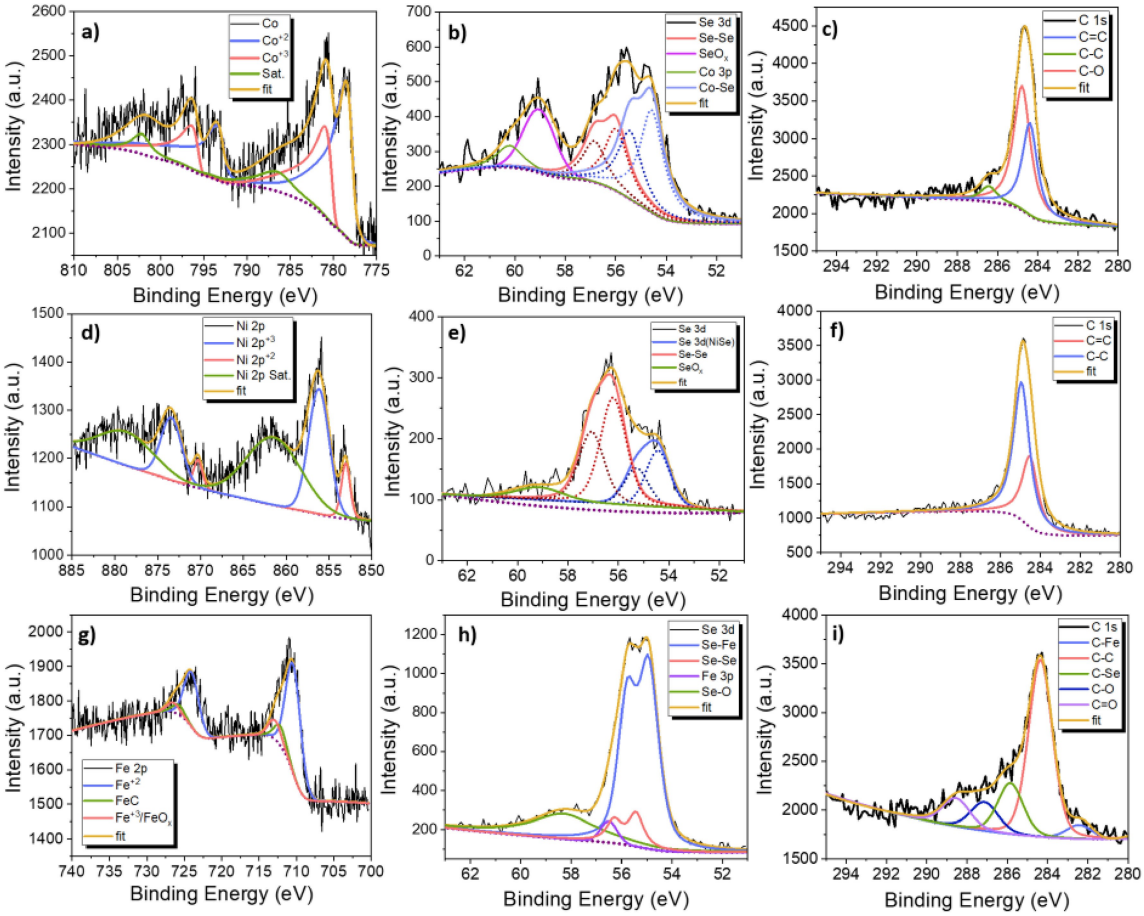

Figure 3. X-Ray Photoelectron Spectroscopy (XPS) high-resolution spectra: **a**, **b**, **c**) for $CoSe_2$/C, **d**, **e**, **f**) Ni for NiSe/C, **g**, **h**, **i**) for FeSe/C composites.

high-resolution carbon spectrum of NiSe/C material are attributed to sp^2 C=C and sp^3 C–C bonds, respectively (Figure 3f).[54] The Fe 2p high-resolution spectrum of the XPS analysis of FeSe/C material in Figure 3g shows the main peaks at 710.42 eV (Fe $2p_{3/2}$) and 723.98 eV (Fe $2p_{1/2}$). The sub-peaks at 710.42 eV and 724.40 eV are associated with the Fe^{2+} peak in FeSe,[61] while the peaks at 712.45 eV and 726.07 eV are associated with Fe^{3+} due to surface oxidation of FeSe.[62] Moreover, the Fe 2p spectrum (712.8 and 725.8 eV) peaks overlapped with iron carbides.[63] As a result of the spectrum and fit obtained from the high-resolution scanning study for the Se element in FeSe material, two peaks at 54.93 eV and 55.79 eV corresponding to Se $3d_{5/2}$ and Se $3d_{3/2}$, respectively, are attributed to the iron-selenium bond structure (Figure 3h). Moreover, the peaks at 55.44 eV and 56.3 eV corresponded to Se $3d_{5/2}$ and $3d_{3/2}$ peaks of elemental selenium. The peak at 59.2 eV also indicated the formation of a Se–O bond resulting from the interaction of selenium with oxygen.[64,65] The peak at 56.5 eV reflects the binding energy of Fe 3p.[66] The sub-peaks obtained as a result of the fit study of the graph obtained by high-resolution photoelectron spectroscopy scanning for the carbon element in the iron selenide material corresponded to C=O (288.54 eV), C–O (287.13 eV), C–Se (285.84 eV) and C–C (284.35 eV), respectively. Finally, the peak at 282.48 eV is attributed to the Fe–C bond (Figure 3i).[67,68] As seen from XPS analysis of metal selenides obtained from MOF selenization, a small amount of unreacted metallic selenium and metal-oxygen bonds were observed in addition to the formation of MSe phases, likely arising from surface oxidation.

A series of electrochemical tests were performed in Na half-cells for transition metal selenides obtained by selenization of gallic acid frameworks. Cyclic voltammetry tests of the cells at a scan rate of 0.1 mV/s in voltage windows from 0.01 V to 3.0 V (vs. Na/Na^+) are shown in Figure 4. In the first scan, there is an irreversible reduction peak around 0.7–0.8 V and 0.3–0.4 V in the cathodic region of each material, which corresponds to the solid electrolyte interface (SEI) layer formation and metal selenide conversion to Na_2Se and metal (Co, Fe, Ni).[69] In the following scans, each material has its own characteristic reduction/oxidation peak regions. For $CoSe_2$/C (Figure 4a), Na^+ addition resulted in the formation of Na_xCoSe_2 (1.4 V) by Na^+ insertion followed by a stepwise conversion reaction at 1.1 V and 0.6 V ($CoSe_2 + xNa^+ + xe^- \rightarrow Na_2Se + Co$).[70,71] For the oxidation reaction, the peak starting at 1.5 V and reaching a maximum at 1.9 V belongs to the adverse desodiation process and formation of $CoSe_2$.[71,72] Similar reduction peaks for nickel selenide appear at 1.3 V and 0.9 V (Figure 4b) due to the decomposition of NiSe to Na_2Se and Ni

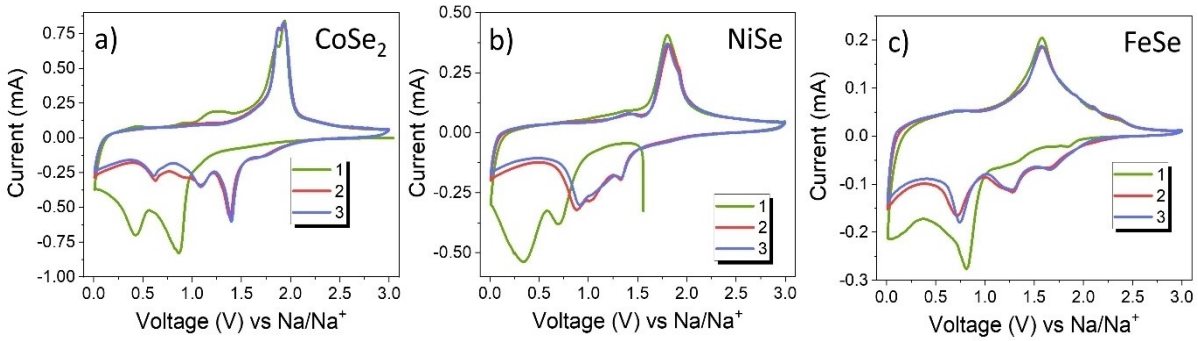

Figure 4. Cyclic voltammetry of metal selenide/carbon composite at a scan rate of 0.1 mV/s, **a**) $CoSe_2$/C, **b**) NiSe/C and **c**) FeSe/C.

$(NiSe + 2Na^+ + 2e^- \rightarrow Na_2Se + Ni)$.[69] In the oxidation region, two peaks visible at 1.4 V and 1.8 V are attributed to the reverse conversion of Ni to NiSe.[73] Finally, in the reduction region of Figure 4c after the first cathodic scan for FeSe, the reduction peaks are observed at 1.7 V, 1.3 V, and 0.7 V, which originated from the intermediate Na_xFeSe formation, reversible SEI at the surface, and the conversion reaction between Na_xFeSe and Na ($FeSe + 2Na^+ + 2e^- \rightarrow Na_2Se + Fe$). In the anodic scan, the peaks at 1.6 V are attributed to the conversion reactions from reduced Fe to FeSe.[74,75]

Figure 5 shows the galvanostatic cycling and C-rate performances of the resulting Co, Ni, and Fe selenides. All three metal selenides had similar electrochemical performance. The formation of the irreversible capacity present in the initial discharge capacities has been attributed to the electrolyte degradation and the formation of the solid electrolyte interface.[76] For the $CoSe_2$/C, the composite obtained an initial discharge capacity of 526 mAh/g and the initial coulombic efficiency (ICE) was calculated as 70% (Figure 5b). For the NiSe/C composite, the initial discharge capacity was 673 mAh/g and in the second cycle, the discharge capacity was 457 mAh/g with 64% ICE (Figure 5e). This was the case for the FeSe/C composite, which had an initial discharge capacity of 521 mAh/g and decreased to a discharge capacity of 387 mAh/g,

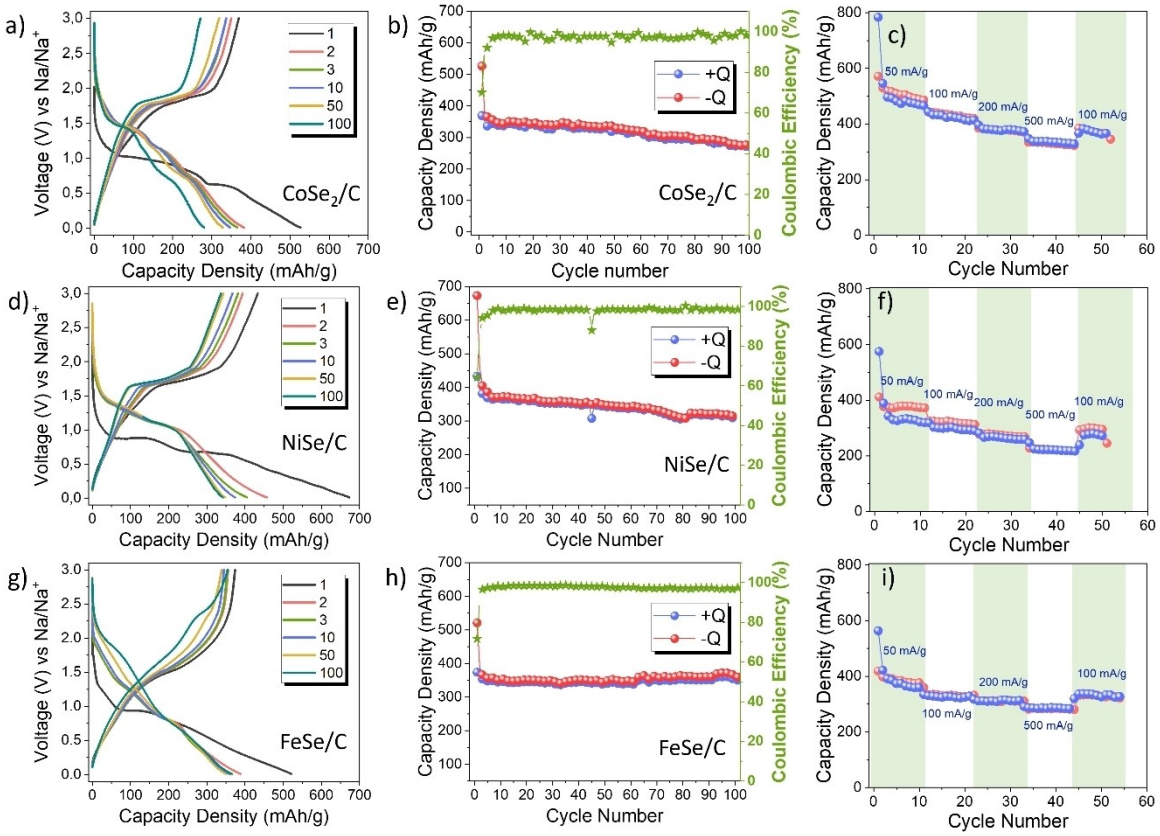

Figure 5. Galvanostatic performance at 100 mA/g current density **a**–**b**) $CoSe_2$/C, **d**–**e**) NiSe/C, and **g**–**h**) FeSe/C and C-rate performances at different current densities **c**) $CoSe_2$/C, **f**) NiSe/C, and **i**) FeSe/C.

maintaining 74% ICE (Figure 5h). The discharge capacities of each material at the end of 100 charge/discharge cycles were 315, 312, and 363 mAh/g for Co, Ni, and Fe selenides, respectively, and maintained 73%, 68%, and 94% of the discharge capacity of 280, 457 mAh/g and 386 mAh/g in the second cycle. Moreover, harsh C-Rate performances were applied to transition metal selenides and they had a capacity of 364, 272, 326 mAh/g in the 50th cycle, which is 82%, 85%, and 98% of the 12th cycle at the current of 100 mAh/g for $CoSe_2$/C, NiSe/C and FeSe/C, respectively (Figure 5c, f, and i). The cells were also tested at higher current density (i.e. 50 mA/g for the first cycle and continued with 500 mA/g) (Figure S5). When comparing the electrode materials ($CoSe_2$/C, NiSe/C, and FeSe/C), no striking performance difference was observed at the lower current density, while some discrepancies were noted at a higher rate, which may be due to differences in the ionic/electronic conductivity, ionic potential and carbon ratios of the composites. For instance, carbon formed by the decomposition of the organic linker was obtained at 600 °C, that may result in low electronic conductivity. The $CoSe_2$/C composite, which has the lowest amount of carbon among the three samples at 9 wt%, may have the optimum ratio to provide sufficient suppression for volume expansion and not further limit electron percolation.

Electrochemical impedance spectroscopy tests were performed at 5 mV amplitude and between 100 kHz and 10 mHz frequencies before and after galvanostatic battery performance at different current densities (Figure S6). The EIS analyses were fit by applying Biologic ZFit based on the equivalent resistance given in Figure S6g. In the Nyquist plot, R1(Rs) obtained at high frequency represents the ohmic resistance of the electrolyte and cell components, the flattened semicircle obtained at high-mid frequency represents the charge transfer resistance Rct = R2 || Q1 and the solid electrolyte interfacial resistance R_{SEI}=R3 || Q2, while the sloping line formed as a straight tail at low-frequency values represents the Warburg component (σ) associated with the diffusion of sodium ions within the active material.[77] The total resistances calculated from the fit data for $CoSe_2$/C, NiSe/C, and FeSe/C materials are 508.8 Ohms, 601.7 Ohms, and 339.8 Ohms for fresh cells, respectively, while the total resistances obtained after the C-rate test are 479 Ohms, 867.5 Ohms, and 620 Ohms, respectively. The changes in resistances after cycling can also be accounted for by modifications in the electrode surface. As seen in the SEM images (Figure S7), selenide-based anode materials with narrow cracks on the fresh cell surfaces became wider after the C-rate performance due to volume expansion.

The galvanostatic intermittent titration technique (GITT) was also used to evaluate the diffusion kinetics of sodium ions in transition metal selenides. Figure 6 shows the GITT curve during a complete discharge/charge process with 20 min galvanostatic discharge/charge and 2 h open circuit rest at a current density of 50 mA/g, and the diffusion coefficient of Na^+ ions was calculated by the equation 2, where τ is the duration of the current pulse (s), nm is the number of moles of the active material, n_m active material mole, V_m is the electrode molar volume (cm^3/mol), S is the electrode surface area (cm^2), ΔE_s is the steady-state potential of the current pulse (V), ΔE_t is the potential change during the constant current pulse after eliminating the iR drop (V) and ΔE_s is steady-state voltage change before and after the current pulse..[70]

$$D_{Na} = \frac{4}{\pi\tau}\left(\frac{n_m V_m}{S}\right)^2\left(\frac{\Delta E_s}{\Delta E_t}\right)^2 \quad (2)$$

According to the GITT profiles, the calculated D_{Na+} for $CoSe_2$/C material was between 1.3×10^{-10} cm^2/s and 2.8×10^{-9} cm^2/s (discharge) (Figure 6c) and between 8.3×10^{-11} cm^2/s and 1.7×10^{-8} cm^2/s (charge) (Figure 6d). The D_{Na+} calculated from the GITT profile of the NiSe/C half-cell is approximately 8.0×10^{-10} cm^2/s to 4.7×10^{-8} cm^2/s (discharge, Figure 6g) and 2.1×10^{-7} cm^2/s to 9.1×10^{-8} cm^2/s during charge (Figure 6h). The sodium diffusion coefficient calculated for FeSe/C has a fluctuating trend between 2.6×10^{-10} cm^2/s and 2.4×10^{-6} cm^2/s (Figure 6k) upon discharge while 3.9×10^{-11} cm^2/s and 5.1×10^{-9} cm^2/s at charging (Figure 6l). There are noticeable fluctuations in D_{Na+} as a function of the voltage profiles of each material. The diffusion coefficient is minimum at 1.4 V, 1.1 V, and 0.8 V during discharge and at 1.8 V and 1.9 V during charging, which is around the voltages at which the phase transformation of $CoSe_2$ occurs.[76,78] This is similar to the D_{Na+} values of NiSe and FeSe materials in the discharge process. Moreover, the diffusion coefficient calculated from the GITT method is generally higher than D_{Na+} calculated from EIS method, due to the different equilibrium conditions.[79] Similar results have been encountered in studies in the literature given in Table S1.

Some transition metal selenides applied as Na-ion anode materials in the literature and their general information are given in Table S2. Their electrochemical performances obtained in this study are presented comparatively. By selenization of MOFs, metal selenide/carbon composites are formed in a single step by both metal selenization and carbonization of organic ligands. This method can shorten the reaction time compared to others and facilitate the homogeneous distribution of the formed metal selenides in the carbon network, thus forming the three-dimensional hierarchical structure of the carbon/active material composites. Although the results of this study are in line with the literature, it differs from other studies in terms of using gallic acid, which is environmentally friendly and can be obtained from natural products, as an organic ligand.

3. Conclusions

This work commenced with a one-step and facile selenization of gallic acid-based metal organic frameworks (Co, Ni, Fe), where the ligand is eco-friendly and produced from biomass. Through simultaneous selenization and carbonization under heat treatment, crystalline $CoSe_2$/C, NiSe/C, and FeSe/C composite materials containing abundant porous amorphous carbon capsules as well as small amounts of unreacted Se were obtained. Electrode resistivity was calculated by electrochemical impedance spectroscopy (EIS) and Na-ion diffusion coefficients

Research Article
doi.org/10.1002/celc.202400385

Chemistry Europe
European Chemical Societies Publishing

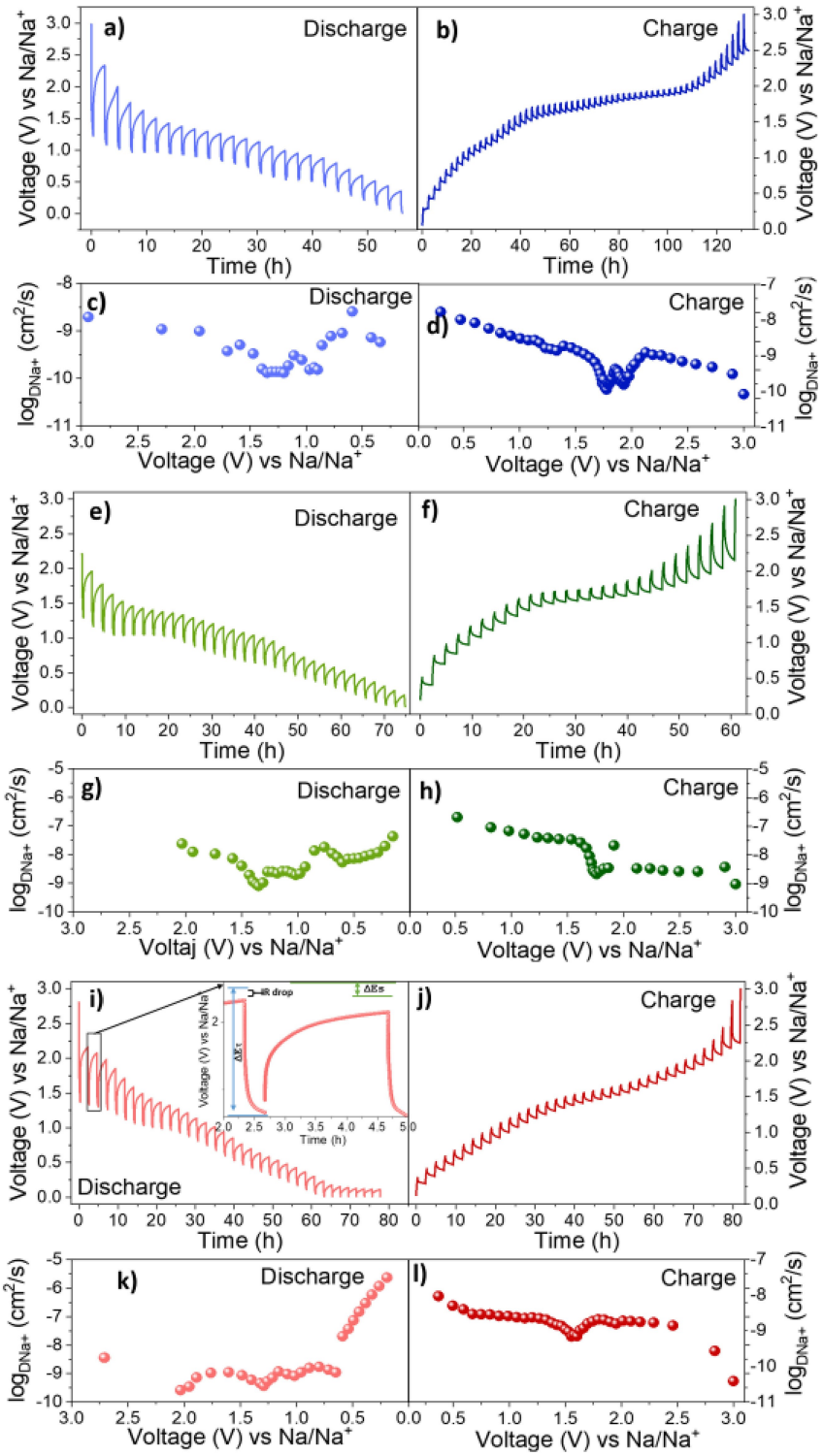

Figure 6. GITT profiles during initial charge and discharge **a**–**b**) $CoSe_2$/C, **e**–**f**) NiSe/C, and **i**–**j**) FeSe/C. Na^+ diffusion coefficient distribution corresponding to a typical charge and discharge curve **c**–**d**) $CoSe_2$/C, **g**–**h**) NiSe and **k**–**l**) FeSe.

were calculated by the GITT technique. Reversible capacity densities of 315 mAh/g ($CoSe_2$), 312 mAh/g (NiSe) and 363 mAh/g (FeSe) were obtained from galvanostatic cycles at a current density of 100 mA/g in the production of sodium ion battery anode materials where carbon encapsulation helps to maintain sustained capacity, and it is emphasized that the MOF-oriented approach promises in the synthesis of electro-active materials.

Acknowledgements

Meral Aydin is supported by the Turkish Higher Education Council's (YÖK) 100/2000 PhD Fellowship Program and 2211/C National PhD Scholarship Program in the Priority Fields in Science and Technology of the Scientific and Technological Research Council of Turkey (TÜBİTAK). Dr. Zeynep Erdöl is thanked for the XRD and SEM measurements. This paper is part of Meral Aydin's PhD dissertation. Several characterizations (PXRD, IR, TGA of MOFs, STEM-EDS analyses) were performed on IMN equipment platform, PLASSMAT, Nantes, France. Funding by the French Contrat Plan État-Région and the European Regional Development Fund of Pays de la Loire, the CIMEN Electron Microscopy Center in Nantes, is greatly acknowledged.

Conflict of Interests

The authors declare no conflict of interest.

Data Availability Statement

The data that support the findings of this study are available from the corresponding author upon reasonable request.

Keywords: Gallic acid · Metal organic framework · Transition metal selenides · Sodium-ion batteries

[1] S. J. An, J. Li, Z. Du, C. Daniel, *J. Power Sources* **2017**, *342*, 846–852.
[2] T. Wang, D. Su, D. Shanmukaraj, T. Rojo, M. Armand, G. Wang, *Electrochem. Energy Rev.* **2018**, *1*, 200–237.
[3] M. D. Slater, D. Kim, E. Lee, C. S. Johnson, *Adv. Funct. Mater.* **2013**, *23*, 947–958.
[4] H. Zhang, I. Hasa, S. Passerini, *Adv. Energy Mater.* **2018**, *8*, 1702582.
[5] M. Aydin, E. Demir, B. Unal, B. Dursun, A. S. Ahsen, R. J. S. Demir-Cakan, *Solid State Ionics* **2019**, *341*, 115035.
[6] E. Canbaz, M. Aydin, R. D. Çakan, *Turk. J. Chem.* **2022**, *46*, 356–366.
[7] M. Dogrusoz, R. Demir-Cakan, *Int. J. Energy Res.* **2020**, *44*, 10809–10820.
[8] M. Aydin, A. S. Ahsen, R. Demir-Cakan, *J. Solid State Electrochem.* **2023**, *27*, 1075–1084.
[9] M. Khan, N. Ahmad, K. Lu, Z. Sun, C. Wei, X. Zheng, R. Yang, *Solid State Ionics* **2020**, *346*, 115223.
[10] M. Yang, X. Chang, L. Wang, X. Wang, M. Gu, H. Huang, L. Tang, Y. Zhong, H. Xia, *Processes* **2023**, *35*, 2208705.
[11] Z.-B. Zhai, K.-J. Huang, X. Wu, *Nano Energy* **2018**, *47*, 89–95.
[12] Z. Xu, Y. Huang, C. Chen, L. Ding, Y. Zhu, Z. Zhang, Z. Guang, *Ceram. Int.* **2020**, *46*, 4532–4542.
[13] Q. Pan, M. Zhang, L. Zhang, Y. Li, Y. Li, C. Tan, F. Zheng, Y. Huang, H. Wang, Q. Li, *ACS Nano* **2020**, *14*, 17683–17692.
[14] Y. Jiang, M. Xie, F. Wu, Z. Ye, Y. Zhang, Z. Wang, Y. Zhou, L. Li, R. Chen, *Small* **2021**, *17*, 2102893.
[15] Y. Feng, M. Xu, T. He, B. Chen, F. Gu, L. Zu, R. Meng, J. Yang, *Adv. Mater.* **2021**, *33*, 2007262.
[16] S. A. He, Z. Cui, Q. Liu, G. He, D. J. Brett, W. Luo, R. Zou, M. Zhu, *Small* **2021**, *17*, 2104186.
[17] C. Zhu, T. Long, B. Feng, C. Wu, Q. Yu, Y. L. Ding, *Small* **2023**, *19*, 2207716.
[18] J. Li, D. Yan, T. Lu, Y. Yao, L. Pan, *Chem. Eng. J.* **2017**, *325*, 14–24.
[19] S. L. James, *Chem. Soc. Rev.* **2003**, *32*, 276–288.
[20] K. Wang, K. N. Hui, K. San Hui, S. Peng, Y. Xu, *Chem. Sci.* **2021**, *12*, 5737–5766.
[21] X. Xu, J. Liu, J. Liu, L. Ouyang, R. Hu, H. Wang, L. Yang, M. Zhu, *Adv. Funct. Mater.* **2018**, *28*, 1707573.
[22] R. A. Bajwa, U. Farooq, S. Ullah, M. Salman, S. Haider, R. Hussain, *J. Storage Mater.* **2023**, *72*, 108708.
[23] M. Dogrusoz, T. Devic, A. Ahsen, R. Demir-Cakan, *Sustain. Energy Fuels* **2021**, *5*, 3363–3372.
[24] B. K. Kang, S. Y. Im, J. Lee, S. H. Kwag, S. B. Kwon, S. Tiruneh, M.-J. Kim, J. H. Kim, W. S. Yang, B. Lim, *Nano Res.* **2019**, *12*, 1605–1611.
[25] L. Liu, X. Meng, L. Hu, S. Liang, L. Yu, D. Liang, L. Wang, N. Zhou, L. Yang, X. Yang, *J. Phys. Chem. C* **2021**, *125*, 15812–15820.
[26] Y. Li, X. Sun, Z. Cheng, X. Xu, J. Pan, X. Yang, F. Tian, Y. Li, J. Yang, Y. Qian, *Energy Storage Mater.* **2019**, *22*, 275–283.
[27] Z. Li, L. Y. Zhang, L. Zhang, J. Huang, H. Liu, *Nanoscale Res. Lett.* **2019**, *14*, 1–11.
[28] H. Fan, H. Yu, X. Wu, Y. Zhang, Z. Luo, H. Wang, Y. Guo, S. Madhavi, Q. Yan, *ACS Appl. Mater. Interfaces* **2016**, *8*, 25261–25267.
[29] T. Meng, J. Qin, S. Wang, D. Zhao, B. Mao, M. Cao, *J. Mater. Chem. A* **2017**, *5*, 7001–7014.
[30] L. Cooper, T. Hidalgo, M. Gorman, T. Lozano-Fernández, R. Simón-Vázquez, C. Olivier, N. Guillou, C. Serre, C. Martineau, F. Taulelle, *Chemical Communications, Vol. 51*, Cambridge **2015**, pp. 5848–5851.
[31] R. Weber, G. Bergerhoff, *Materials (Basel)* **1991**, *195*, 87–88.
[32] R. K. Feller, A. K. Cheetham, *Solid State Sci.* **2006**, *8*, 1121–1125.
[33] P. J. Saines, H. H.-M. Yeung, J. R. Hester, A. R. Lennie, A. K. Cheetham, *Transactions* **2011**, *40*, 6401–6410.
[34] J. Chen, Y. Chen, S. Li, J. Yang, J. Dong, *Colloids Surf. A* **2022**, *650*, 129318.
[35] Z. Li, Z. Jiang, W. Zhu, C. He, P. Wang, X. Wang, T. Li, L. Tian, *Appl. Surf. Sci.* **2020**, *504*, 144368.
[36] Y. Liu, T. Sakthivel, F. Hu, Y. Tian, D. Wu, E. H. Ang, H. Liu, S. Guo, S. Peng, Z. Dai, *Adv. Energy Mater.* **2023**, *13*, 2203797.
[37] A. Jana, M. Hazra, J. Datta, *ACS Appl. Energy Mater.* **2018**, *2*, 232–242.
[38] J. K. Kim, G. D. Park, J. H. Kim, S. K. Park, Y. C. Kang, *Small* **2017**, *13*, 1700068.
[39] Z. Zhang, X. Shi, X. Yang, *Electrochim. Acta* **2016**, *208*, 238–243.
[40] Y. Tang, Z. Zhao, X. Hao, Y. Wang, Y. Liu, Y. Hou, Q. Yang, X. Wang, J. Qiu, *J. Mater. Chem. A* **2017**, *5*, 13591–13600.
[41] S. H. Yang, S.-K. Park, Y. C. Kang, *Chem. Eng. J.* **2019**, *370*, 1008–1018.
[42] R. Bardestani, G. S. Patience, S. Kaliaguine, *Can. J. Chem. Eng.* **2019**, *97*, 2781–2791.
[43] X. Hu, *J. Mater. Chem. A* **2019**, *7*(11018), 11016–11037.
[44] J. Lin, J. He, F. Qi, B. Zheng, X. Wang, B. Yu, K. Zhou, W. Zhang, Y. Li, Y. Chen, *Electrochim. Acta* **2017**, *247*, 258–264.
[45] S. Kukunuri, M. R. Krishnan, S. Sampath, *Phys. Chem. Chem. Phys.* **2015**, *17*, 23448–23459.
[46] P. Jing, Q. Wang, C. Xian, L. Du, Y. Zhang, B. Wang, H. Wu, K. Wu, Q. Wang, Y. Zhang, *Inorg. Chem. Front.* **2021**, *8*, 3686–3696.
[47] K. Chhetri, B. Dahal, A. P. Tiwari, T. Mukhiya, A. Muthurasu, G. P. Ojha, M. Lee, T. Kim, S.-H. Chae, H. Y. Kim, *ACS Appl. Energy Mater.* **2020**, *4*, 404–415.
[48] W. Song, K. Wang, G. Jin, Z. Wang, C. Li, X. Yang, C. Chen, *ChemElectroChem* **2019**, *6*, 4842–4847.
[49] J. Li, Q. He, Y. Lin, L. Han, K. Tao, *Inorg. Chem.* **2022**, *61*, 19031–19038.
[50] Z. Liu, D. Gao, L. Hu, H. Liu, Y. Li, Y. Xue, F. Liu, J. Zhang, C. Tang, *Colloids Surf. A* **2022**, *646*, 128903.
[51] F. Xie, Z. Xu, Z. Y. Guo, Y. X. Lu, L. Q. Chen, M. M. Titirici, Y. S. Hu, *Sci. China Chem.* **2021**, *64*, 1679–1692.
[52] X. Yang, S. Wang, Y. Denis, A. L. Rogach, *Nano Energy* **2019**, *58*, 392–398.
[53] Y. Zhou, H. Xiao, S. Zhang, Y. Li, S. Wang, Z. Wang, C. An, J. Zhang, *Electrochim. Acta* **2017**, *241*, 106–115.
[54] X. Chen, X. Wang, D. Fang, *Fullerenes Nanotubes Carbon Nanostruct.* **2020**, *28*, 1048–1058.
[55] H. Nesbitt, D. Legrand, G. Bancroft, *Phys. Chem. Miner.* **2000**, *27*, 357–366.
[56] A. Mandale, S. Badrinarayanan, S. Date, A. Sinha, *J. Electron Spectrosc. Relat. Phenom.* **1984**, *33*, 61–72.
[57] Y. Guo, K. Jia, F. Dai, Y. Liu, C. Zhang, J. Su, K. Wang, *J. Colloid Interface Sci.* **2023**, *642*, 638–647.
[58] J. Liang, Y. Yang, J. Zhang, J. Wu, P. Dong, J. Yuan, G. Zhang, J. Lou, *Nanoscale Res. Lett.* **2015**, *7*, 14813–14816.
[59] F. Wang, Y. Li, T. A. Shifa, K. Liu, F. Wang, Z. Wang, P. Xu, Q. Wang, J. He, *Angew. Chem. Int. Ed.* **2016**, *55*, 6919–6924.
[60] J. Fan, Y. Zeng, J. Sun, *J. Soils Sediments* **2018**, *18*, 2935–2947.
[61] Y. Xiao, J.-Y. Hwang, I. Belharouak, Y.-K. Sun, *ACS Energy Lett.* **2017**, *2*, 364–372.
[62] Y. Cao, S. Huang, Z. Peng, F. Yao, X. Li, Y. Liu, H. Huang, M. Wu, *J. Mater. Chem. A* **2021**, *9*, 3464–3471.

[63] Y. Liu, P. R. Murthy, X. Zhang, H. Wang, C. Shi, *New J. Chem.* **2021**, *45*, 22444–22449.
[64] A. Naveau, F. Monteil-Rivera, E. Guillon, J. Dumonceau, *Environ. Sci. Technol. Health Care* **2007**, *41*, 5376–5382.
[65] F. A. Perras, S. Hwang, Y. Wang, E. C. Self, P. Liu, R. Biswas, S. Nagarajan, V. H. Pham, Y. Xu, J. A. Boscoboinik, *Nano Lett.* **2019**, *20*, 918–928.
[66] L. Xu, F. Fu, *J. Environ. Sci. Health Part A* **2020**, *55*, 528–536.
[67] G. Panzner, W. Diekmann, *Surf. Sci.* **1985**, *160*, 253–270.
[68] Y. Li, Y. Xu, Z. Wang, Y. Bai, K. Zhang, R. Dong, Y. Gao, Q. Ni, F. Wu, Y. Liu, *Adv. Energy Mater.* **2018**, *8*, 1800927.
[69] J. Liu, Z. Leng, H. Dong, X. Xu, C. Lv, H. Wei, L. Yu, J. Yang, H. Geng, *Inorg. Chem. Front.* **2023**, *10*, 4076–4086.
[70] K. Zhang, M. Park, L. Zhou, G. H. Lee, W. Li, Y. M. Kang, J. Chen, *Adv. Funct. Mater.* **2016**, *26*, 6728–6735.
[71] H. Yin, H.-Q. Qu, Z. Liu, R.-Z. Jiang, C. Li, M.-Q. Zhu, *Nano Energy* **2019**, *58*, 715–723.
[72] J. Sun, D. Ji, H. Ye, B. Yu, Y. Wang, S. Ramakrishna, L. Lu, *Cell Rep. Phys. Sci.* **2020**, *1*, 1–13.
[73] Y. Liu, X. Wang, *Mater. Corros.* **2019**, *12*, 3709.
[74] Q. Li, H. D. Wang, H. G. Wang, Z. J. Si, C. P. Li, J. Bai, *ChemSusChem* **2020**, *13*, 2449–2456.
[75] K. Wu, F. Chen, Z. Ma, B. Guo, Y. Lyu, P. Wang, H. Yang, Q. Li, H. Wang, A. Nie, *Chem. Commun.* **2019**, *55*, 5611–5614.
[76] B. Cong, X. Li, Y. Suo, G. Chen, *J. Colloid Interface Sci.* **2023**, *635*, 370–378.
[77] B. Jin, E. M. Jin, K.-H. Park, H.-B. Gu, *Electrochem. Commun.* **2008**, *10*, 1537–1540.
[78] G. Fang, Z. Wu, J. Zhou, C. Zhu, X. Cao, T. Lin, Y. Chen, C. Wang, A. Pan, S. Liang, *Adv. Energy Mater.* **2018**, *8*, 1703155.
[79] S. Rajput, A. K. Panwar, A. Gupta, *Solid State Ionics* **2023**, *394*, 116206.

Manuscript received: May 27, 2024
Revised manuscript received: July 29, 2024
Version of record online: ■■, ■■

RESEARCH ARTICLE

Transition metal (Co, Ni, and Fe) selenides are obtained from one-step selenization of gallic acid-based metal-organic frameworks (MOFs). The resulting nanomaterials are employed as sodium-ion battery anodes with encouraging results.

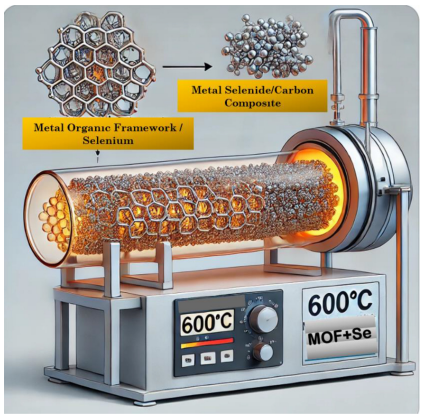

*M. Aydin, T. Devic, A. Şems Ahsen, N. Gautier, R. Demir-Cakan**